Tunability of the topological nodal-line semimetal phase in ZrSiX-type materials (X = S, Se, Te)

M. Mofazzel Hosen,[1] Klauss Dimitri,[1] Ilya Belopolski,[2] Pablo Maldonado,[3] Raman Sankar,[4,5] Nagendra Dhakal,[1] Gyanendra Dhakal,[1] Taiason Cole,[1] Peter M. Oppeneer,[3] Dariusz Kaczorowski,[6] Fangcheng Chou,[5] M. Zahid Hasan,[2] Tomasz Durakiewicz,[7,8] and Madhab Neupane[1,*]

[1]*Department of Physics, University of Central Florida, Orlando, Florida 32816, USA*
[2]*Joseph Henry Laboratory and Department of Physics, Princeton University, Princeton, New Jersey 08544, USA*
[3]*Department of Physics and Astronomy, Uppsala University, P.O. Box 516, S-75120 Uppsala, Sweden*
[4]*Institute of Physics, Academia Sinica, Taipei 10617, Taiwan*
[5]*Center for Condensed Matter Sciences, National Taiwan University, Taipei 10617, Taiwan*
[6]*Institute of Low Temperature and Structure Research, Polish Academy of Sciences, PL-50-950 Wroclaw, Poland*
[7]*Condensed Matter and Magnet Science Group, Los Alamos National Laboratory, Los Alamos, New Mexico 87545, USA*
[8]*Institute of Physics, Maria Curie-Sklodowska University, PL-20-031 Lublin, Poland*

The discovery of a topological nodal-line (TNL) semimetal phase in ZrSiS has invigorated the study of other members of this family. Here, we present a comparative electronic structure study of ZrSiX (where X = S, Se, Te) using angle-resolved photoemission spectroscopy (ARPES) and first-principles calculations. Our ARPES studies show that the overall electronic structure of ZrSiX materials comprises the diamond-shaped Fermi pocket, the nearly elliptical-shaped Fermi pocket, and a small electron pocket encircling the zone center (Γ) point, the M point, and the X point of the Brillouin zone, respectively. We also observe a small Fermi surface pocket along the M-Γ-M direction in ZrSiTe, which is absent in both ZrSiS and ZrSiSe. Furthermore, our theoretical studies show a transition from nodal-line to nodeless gapped phase by tuning the chalcogenide from S to Te in these material systems. Our findings provide direct evidence for the tunability of the TNL phase in ZrSiX material systems by adjusting the spin-orbit coupling strength via the X anion.

Topological insulators (TIs) are bulk insulating systems with gapless robust surface states originating from a nontrivial electronic band structure [1–6]. These systems are on the frontier of research interests of modern condensed matter physics. Recently, semimetals such as the Dirac semimetal, Weyl semimetal, and nodal-line semimetal have been reported to also exhibit this novel nontrivial topological state [7–34]. The Dirac and Weyl semimetals possess symmetry-protected zero-dimensional (0D) band touching near the Fermi level [7–19,25]. These states have been experimentally demonstrated in many materials such as Cd_3As_2 [7–11], Na_3Bi [30–33], TaAs [15–18], NdSb [35], WTe_2 [36–38], etc. Their low-energy bulk band structure contains linearly dispersive bands, leading to unusual exotic transport behaviors such as extremely high bulk carrier mobility and extreme magnetoresistance as a consequence of the chiral anomaly [39–42]. Moreover, nodal-line semimetals show extended lines such as one-dimensional (1D) band touching loops or lines in momentum (k) space. These 1D loops or lines need extra symmetries to protect them, aside from the translational symmetry, and show many anomalous properties in transport measurements [20–29]. To date, several materials such as $PbTaSe_2$ [43], $PtSn_4$ [44], and ZrSiS [26,27] have been experimentally reported to host this novel state.

The recently reported ZrSiS is an interesting material because it exhibits multiple Dirac cones as well as the nodal-line semimetal phase [26,27]. Importantly, the Dirac bands in this material show a linear dispersion behavior over a large energy range of up to 2 eV. Furthermore, a single layer of this material is predicted to host the 2D TI electronic structure [14,25]. The nodal-line semimetal phase in ZrSiS was reported assuming a negligible spin-orbit coupling (SOC) strength [26,27]. Hence, by tuning the chalcogenide from S to Te, while maintaining the isoelectronic properties but by increasing the atomic number (Z) of the chalcogen ion, one can play with the SOC strength to investigate the possible tunability of the nodal phase in this material system. Recently, the existence of the topological nodal-line semimetal phase in ZrSiSe and ZrSiTe as well as the 3D to 2D structural transition in ZrSiTe have been suggested [45]. The two compounds ZrSiSe and ZrSiTe have a layered crystal structure similar to ZrSiS but with a different SOC strength. However, the details of the electronic structure as well as the effect of SOC have yet to be reported in these material systems using momentum-resolved spectroscopic probe and first-principles band-structure calculations.

Here, we present a comparative electronic structure study of ZrSiX (where X = S, Se, Te) using angle-resolved photoemission spectroscopy (ARPES) and first-principles calculations to reveal the effect of SOC on their band structures. Our ARPES measurements show that the overall electronic structures are the same for ZrSiS, ZrSiSe, and ZrSiTe, but the details of their electronic structure show subtle but important differences. We observe a diamond-shaped Fermi surface around the zone center (Γ) point, a nearly elliptical-shaped Fermi pocket around the M point, and a small electronic pocket at the corner (X) point of the Brillouin zone (BZ) in ZrSiSe and ZrSiTe. However, in ZrSiTe an additional small pocket is observed in the M-Γ-M momentum space direction. Furthermore, we observe linearly dispersive surface states in both materials around the X point of the BZ. These experimental observations

---

*Corresponding author: mneupane2002@gmail.com

are further supported by our first-principles band-structure calculations. Our theoretical band-structure calculation shows a negligible gap at ZrSiSe and an approximately 60 meV gap in ZrSiTe around the M-Γ-M (nodal-line) direction in the BZ. This gap opening is attributed to the higher SOC effect in ZrSiTe. Our findings provide a platform to observe the tunable nodal-line semimetal phase in the ZrSiX material system.

The single crystals of ZrSiSe and ZrSiTe were grown by the vapor transport method as described elsewhere [46,47]. Their chemical composition was checked by energy-dispersive x-ray analysis using a FEI scanning electron microscope equipped with an EDAX Genesis XM4 spectrometer. The results indicated homogeneous single-phase materials with their stoichiometry close to equiatomic. Single-crystal x-ray diffraction (XRD) experiments were performed on a Kuma-Diffraction KM4 four-circle diffractometer equipped with a CCD camera using Mo $K\alpha$ radiation. Rietveld refinements of the XRD data yielded the tetragonal space group $P4/nmm$ with the lattice parameters close to those reported in the literature [46]. Electrical resistivity measurements were carried out within the temperature range 2–300 K and in applied magnetic fields up to 9 T using a conventional four-point ac technique implemented in a Quantum Design physical properties measurement system (PPMS) platform. The electrical contacts to as-grown crystals were made using a silver epoxy paste. The electrical resistivity of ZrSiSe and ZrSiTe was measured with electrical current flowing within the basal plane of their tetragonal unit cells. Synchrotron-based ARPES measurements of the electronic structure were performed at the SIS-HRPES end station of the Swiss Light Source (SLS) and Advanced Light Source (ALS) BL 4.0.1 with Scienta R4000 and R8000 hemispherical

electron analyzers. The energy resolution was set to be better than 20 meV and the angular resolution was set to be better than 0.2° for these measurements. The electronic structure calculations were carried out using the Vienna *ab initio* simulation package (VASP) [48,49], with the generalized gradient approximation (GGA) as the density functional theory exchange-correlation functional [50]. Projector augmented-wave pseudopotentials [51] were used with an energy cutoff of 500 eV for the plane-wave basis, which was sufficient to converge the total energy for a given k-point sampling. In order to simulate surface effects, we used a $1 \times 1 \times 5$ supercell for the (010) surface, with a vacuum thickness larger than 19 Å. The Brillouin zone integrations were performed on a special k-point mesh generated by a $25 \times 25 \times 25$ and a $40 \times 40 \times 1$ Γ-centered Monkhorst Pack k-point grid for the bulk and surface calculations, respectively. The SOC was included self-consistently in the electronic structure calculations.

We start our discussion by presenting the crystal structures of ZrSiSe and ZrSiTe. Similar to the ZrSiS structure, they also crystallize in a PbFCl-type crystal structure with space group $P4/nmm$ [46]. Zr layers are separated by two neighboring X atoms layers, and sandwiched between a Si square net [see Fig. 1(a)]. The bond between Zr-X is relatively weak, and it provides a natural cleavage plane between two neighboring Zr-Se or Zr-Te terminals. The crystal easily cleaves along the (001) surface. Figure 1(b) shows the core level measurements of ZrSiSe and ZrSiTe. The red curve represents the spectroscopic core level measurement of ZrSiSe and the blue curve represents the core level measurement of ZrSiTe. We observe a peak of Zr 4p around 27 eV for both materials, and sharp peaks of Te $4d_{5/2}$ (~40.7 eV), Te $4d_{3/2}$ (~42 eV) of ZrSiTe,
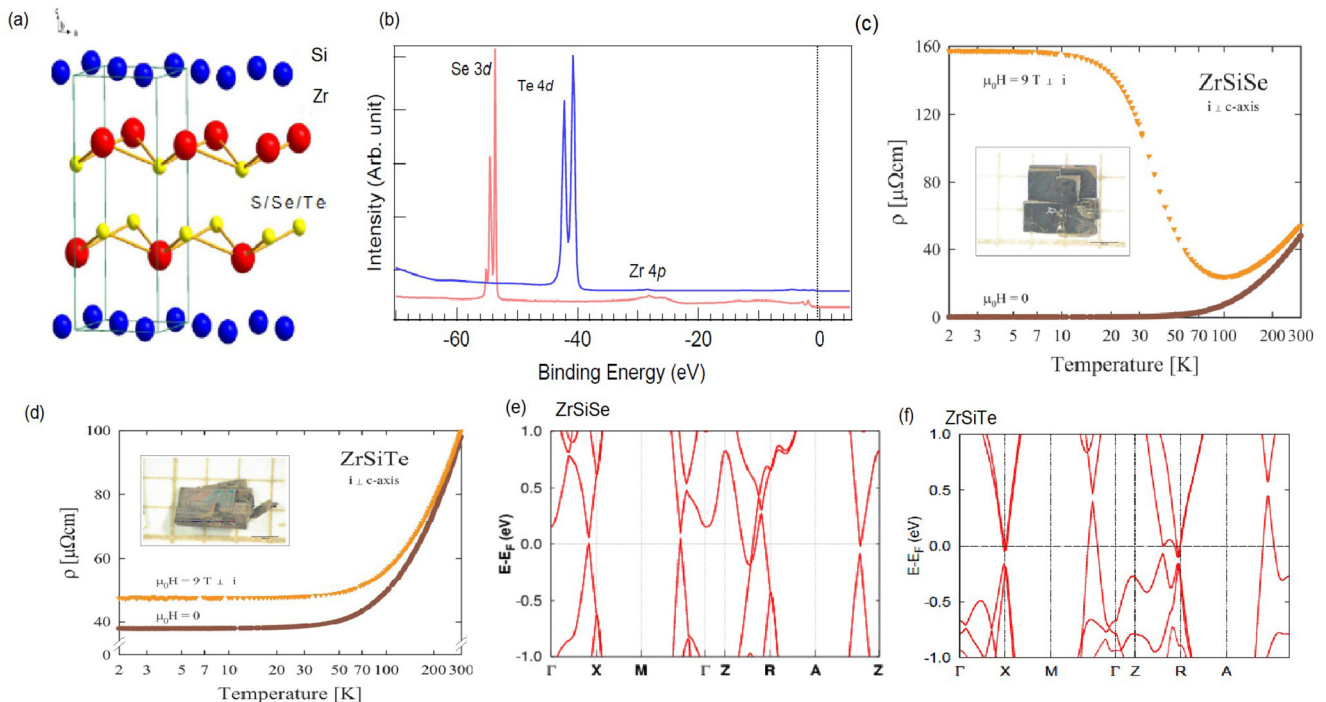

FIG. 1. Crystal structure and sample characterization. (a) Tetragonal crystal structure of ZrSiX (X = S, Se, Te). (b) Core level spectroscopic measurements for ZrSiSe (red curve) and ZrSiTe (blue curve). (c), (d) Sample picture and temperature-dependent resistivity plot with current along the *ab* direction of ZrSiSe and ZrSiTe, respectively. (e), (f) Calculated band structures of ZrSiSe and ZrSiTe along high-symmetry directions, with symmetry points indicated.
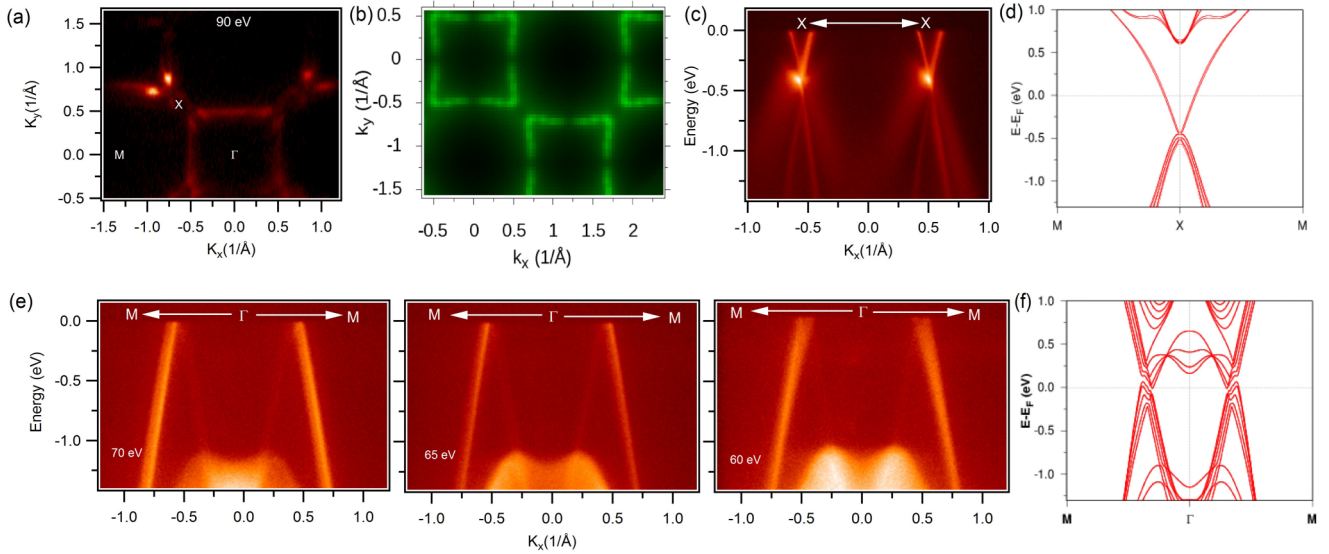
FIG. 2. Electronic structure of ZrSiSe. (a) Fermi surface map measured with a photon energy of 90 eV. High-symmetry points are noted. (b) Calculated Fermi surface cross section. (c) Dispersion map along the X-X direction. (d) Band dispersion obtained from slab calculations along the M-X-M direction. (e) Photon energy-dependent ARPES dispersion along the M-Γ-M direction. The photon energies are also marked in the figures. (f) Calculated bands along the M-Γ-M direction. ARPES measurements presented in this figure were performed at ALS BL 4.0.1 at a temperature of 18 K.

and Se $3d$ ($\sim$55 eV) of ZrSiSe. It indicates that the sample used for our measurements is of good quality. Figures 1(c) and 1(d) display the temperature variations of the electrical resistivity of single-crystalline ZrSiSe and ZrSiTe, respectively, measured with electrical current flowing within the basal plane of their tetragonal unit cells ($i \perp c$ axis). In a zero magnetic field, both compounds exhibit metallic conductivity. For ZrSiSe, the ratio of the room-temperature resistivity to the residual resistivity of 0.3 $\mu\Omega$ cm observed at 2 K was about 160, proving the excellent quality of the single crystal studied. In the case of ZrSiTe, these two quantities were 38 $\mu\Omega$ cm and 2.6, respectively, which might signal possible atomic disorder in the crystal lattice. Another plausible explanation of this result is some oxidation of the surface of the measured specimen that resulted in worse electrical contacts (we observed that crystals of the telluride, in contrast to those of ZrSiS and ZrSiSe, are fairly unstable against air and moisture). In a magnetic field applied perpendicular to the electrical current, the electrical resistivity of ZrSiSe changes in a previously reported manner for topologically nontrivial semimetals, such as WTe$_2$ [36,38], LaSb [52], and TaAs$_2$ [53].

The characteristic upturn in $\rho(T)$ followed by a plateau at low temperatures can be attributed to magnetic-field-driven changes in charge carrier densities and mobilities in a system close to nearly perfect electron-hole compensation [54]. An alternative explanation for the observed behavior is a magnetic-field-induced metal-insulator transition in Dirac systems [36]. In a field of 9 T, the transverse ($H \perp i$) magnetoresistance (MR) of ZrSiSe, defined as MR = $[\rho(T,H) - \rho(T,0)]/\rho(T,0)$, reaches a giant value of about 48 000% at 2 K. With increasing temperature, it systematically decreases down to 13% at 300 K. In contrast to the selenide, ZrSiTe exhibits ordinary magnetotransport, characterized by positive MR values of 26% at 2 K and 3% at 300 K, in a field of 9 T. This behavior hints at the prevalence of one type of carrier which

determines the electrical conductivity of the system. Figure 1(e) shows the band structure of ZrSiSe calculated by including the SOC, along various high-symmetry directions in the BZ. A negligible gap is found at the M-Γ-M direction. Furthermore, compared to the previously reported band calculation of ZrSiS [26,27], bands are shifted towards the chemical potential at various high-symmetry points. Figure 1(f) shows the calculated band structure of ZrSiTe. Compared to ZrSiSe [see Fig. 1(e)], some bands are shifted upward and others downward around the various high-symmetry points.

In order to determine the details of the electronic structure of ZrSiSe and ZrSiTe, we present our systematic surface electronic structure studies in Figs. 2 and 3. Figure 2(a) shows the ARPES measured Fermi surface map at a photon energy of 90 eV at a temperature of 18 K. We observe a diamond-shaped Fermi surface around the Γ points, a nearly elliptical-shaped Fermi pocket around the M point, and a small circular electron pocket at the X point of the BZ, which is in agreement with the previously established electronic structure of ZrSiS [26,27]. The high-symmetry points are also denoted in the figure. Figure 2(b) shows the calculated Fermi surface. The calculated Fermi surface shows good agreement with the experimental observation. Figure 2(c) shows the dispersion map along the X-X direction measured with a photon energy of 65 eV. The Dirac point is observed nearly 400 meV below the chemical potential. One possible reason behind this brightness could be the matrix element effect. Figure 2(d) shows the calculated bands along the M-X-M direction. The photon energy-dependent ARPES dispersion along the high-symmetry M-Γ-M direction is presented in Fig. 2(e). These states originate from the nodal-line state, and show excellent agreement with our calculation in Fig. 2(f). The nodal-line points from our measured dispersion maps are not visible along this direction (M-Γ-M) as these are located above the observed chemical potential. We note that the linearly
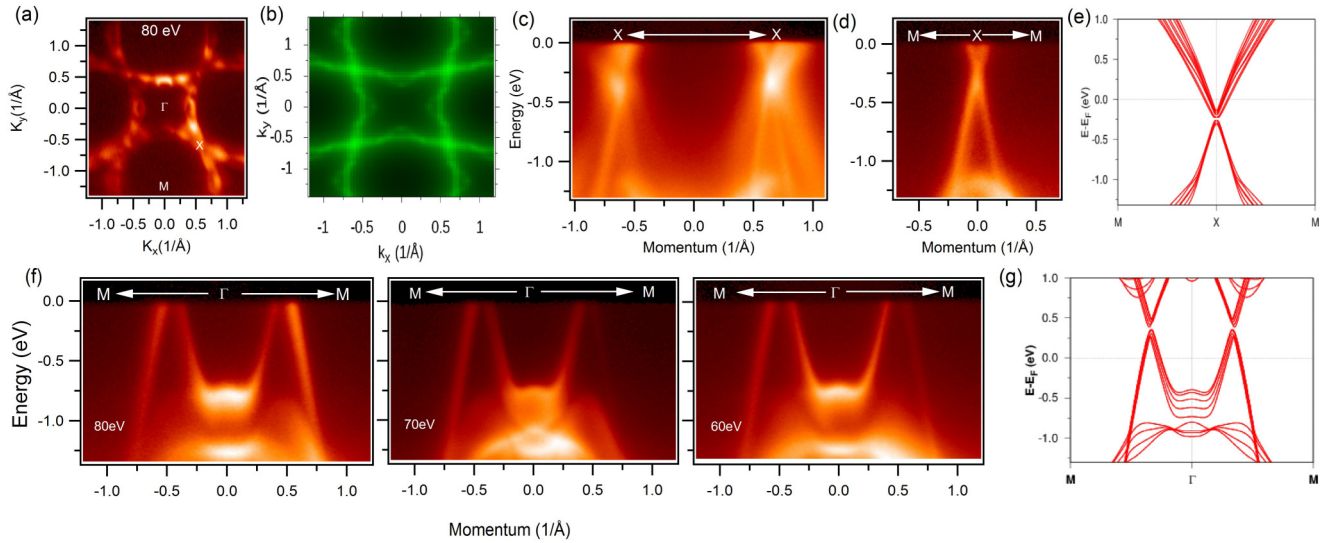
FIG. 3. Electronic structure of ZrSiTe. (a) Fermi surface measured with a photon energy of 80 eV. High-symmetry points are noted in the plot. (b) Calculated Fermi surface map. (c) Dispersion map along the X-X direction measured with photon energy of 60 eV. (d) Measured dispersion map along the M-X-M direction. (e) Calculated bands along the M-X-M direction. (f) Photon energy-dependent dispersion maps along the M-Γ-M direction. Photon energies are mentioned in the plots. (g) Calculation showing the dispersion map along the M-Γ-M high-symmetry direction. These data were collected at the SIS-HRPES end station at SLS at a temperature of 18 K.

dispersive band energy range is larger than 1 eV below the chemical potential.

In Fig. 3 we present our electronic structure study of ZrSiTe. Figure 3(a) presents the Fermi surface map of ZrSiTe measured with a photon energy of 80 eV and a temperature of 18 K. The overall electronic structure of ZiSiTe is similar to that of ZrSiS and ZrSiSe. Interestingly, additional small pockets are observed along the M-Γ-M directions of the BZ. Figure 3(b) shows the calculated Fermi surface, which is in good agreement with the experimental Fermi surface. The measured ARPES dispersion along the X-X direction is presented in Fig. 3(c). Figure 3(d) shows the measured dispersion along the M-X-M direction. The Dirac point is observed around 300 meV below the chemical potential on both plots. Calculated bands along the M-X-M direction are shown in Fig. 3(e). We note that the location of the Dirac point about the X point in ZrSiSe is 400 meV below the chemical potential [see Fig. 2(c)] whereas that one for ZrSiTe is about 300 meV [see Figs. 3(c) and 3(d)]. Figure 3(f) presents the measured photon energy-dependent dispersion maps along the M-Γ-M direction. Experimentally measured dispersion maps agree well with the calculated band dispersion along the M-Γ-M direction as shown in Fig. 3(g). We observe that the linearly dispersive band along this direction extends as far as 1 eV below the chemical potential.

To compare the electronic structures, we show the constant energy contour plots and Fermi surface maps of ZrSiX where $X =$ S, Se, Te, in Fig. 4. Our systematic studies show that ZrSiSe has a similar electronic structure to ZrSiS [26,27] but ZrSiTe possesses some different features, such as a small pocket along the M-Γ-M direction. Figure 4(a) shows a plot of the Fermi surface map of ZrSiSe (left) and several constant energy contours measured with various binding energies as noted in the plots, which are measured at a photon energy of 80 eV and a temperature of around 18 K. Experimentally,

we observe a diamond-shaped Fermi surface [Fig. 4(a), left]. The Dirac point is observed at the X point of the Fermi surface at around 400 meV below the Fermi level (FL) [see Fig. 4(a), right]. Moving towards higher binding energies, the diamond-shaped Fermi surface with gapped out Dirac points becomes disconnected, and the structure resembles a diamond within a diamond, as seen in Fig. 4(a) (right). The inner diamond shape is clearly disconnected along the M-Γ-M directions. Figure 4(b) shows the Fermi surface map (left) and constant energy contour plots (right) of ZrSiTe at a photon energy of 80 eV. A similar diamondlike shape is observed with extra small pockets, and a Dirac pointlike state is observed at the X points nearly 300 meV below the chemical potential. Moreover, we notice that the half-circular-like pocket size is enlarging with the increase of the binding energy, indicating its holelike nature. Furthermore, we performed measurements of Fermi surface mapping at various photon energies (see Supplemental Material [55]), which show that holelike pockets do not disperse with photon energy [45]. Figures 4(c)–4(e) present the Fermi surface maps of ZrSiS (90 eV), ZrSiSe (80 eV), and ZrSiTe (90 eV) using ARPES. Approaching ZrSiTe from ZrSiS, we observe a similar kind of diamond-shaped Fermi surface with some extra features added in ZrSiTe. The same subtle differences are also observed in our band-structure calculations. Furthermore, we observe a gapped out nodal-line phase in ZrSiTe compared to the negligible gap observed in ZrSiSe.

In conclusion, we have performed a comparative electronic structure study of the ZrSiX system using ARPES and first-principles calculations. Our experimental data reveal the overall similarities among the electronic structures of ZrSiX with an additional feature of a small hole pocket in ZrSiTe, which is complemented by our first-principles calculations. Importantly, our theoretical study reveals the exciting possibility of the continuous transition of the topological nodal-line
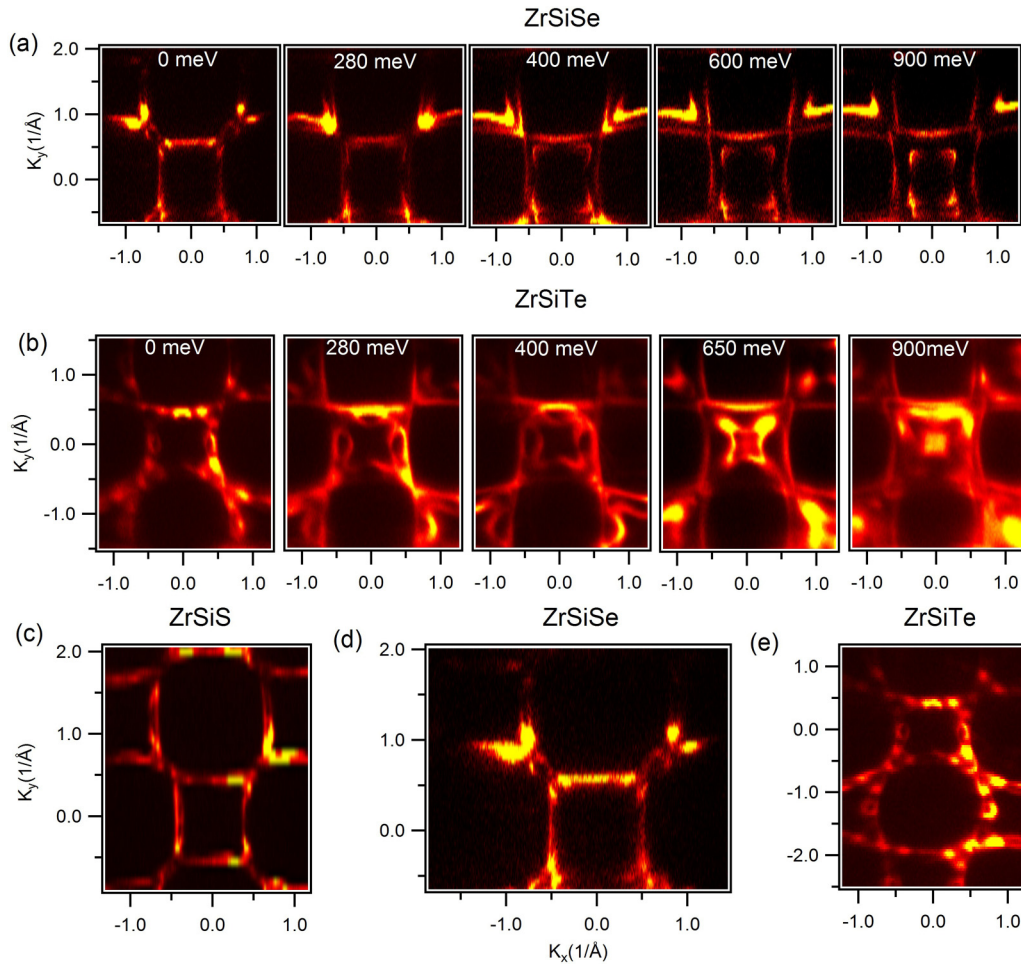
FIG. 4. Comparison of the electronic structures of ZrSiS, ZrSiSe, and ZrSiTe. Fermi surface (0 meV) and constant energy contour maps of (a) ZrSiSe and (b) ZrSiTe. The binding energy values are given in the plots. (c)–(e) ARPES measured Fermi surface for ZrSiS, ZrSiSe, and ZrSiTe, respectively.

semimetal fermion phase to the nodeless gapped out semimetal phase in these systems by tuning the chalcogen element of these materials. The changing SOC effect can be the reason behind this gap opening when the system moves from ZrSiS to ZrSiTe. Our studies reveal the systematic electronic structure of ZrSiX, and establish a material system with an SOC tunable nodal-line phase.

[1] M. Z. Hasan and C. L. Kane, Rev. Mod. Phys. **82**, 3045 (2010).

[2] X.-L. Qi and S.-C. Zhang, Rev. Mod. Phys. **83**, 1057 (2011).

[3] D. Hsieh, D. Qian, L. Wray, Y. Q. Xia, Y. S. Hor, R. J. Cava, and M. Z. Hasan, Nature (London) **452**, 970 (2008).

[4] Y. Xia, D. Qian, D. Hsieh, L. Wray, A. Pal, H. Lin, A. Bansil, D. Grauer, Y. S. Hor, R. J. Cava, and M. Z. Hasan, Nat. Phys. **5**, 398 (2009).

[5] M. Neupane, A. Richardella, J. Sanchez-Barriga, S. Y. Xu, N. Alidoust, I. Belopolski, C. Liu, G. Bian, D. Zhang, D. Marchenko *et al.*, Nat. Commun. **5**, 3841 (2014).

[6] M. Z. Hasan, S.-Y. Xu, and M. Neupane, *Topological Insulators: Fundamentals and Perspectives* (Wiley, New York, 2015).

[7] Z. Wang, H. Weng, Q. Wu, X. Dai, and Z. Fang, Phys. Rev. B **88**, 125427 (2013).

[8] M. Neupane, S.-Y. Xu, R. Sankar, N. Alidoust, G. Bian, C. Liu, I. Belopolski, T.-R. Chang, H.-T. Jeng, H. Lin *et al.*, Nat. Commun. **5**, 3786 (2014).

[9] S. Borisenko, Q. Gibson, D. Evtushinsky, V. Zabolotnyy, B. Büchner, and R. J. Cava, Phys. Rev. Lett. **113**, 027603 (2014).

[10] Y. Zhao, H. Liu, C. Zhang, H. Wang, J. Wang, Z. Lin, Y. Xing, H. Lu, J. Liu, Y. Wang, S. M. Brombosz, Z. Xiao, S. Jia, X. C. Xie, and J. Wang, Phys. Rev. X **5**, 031037 (2015).

[11] H. Wang, H. Wang, H. Liu, H. Lu, W. Yang, S. Jia, X.-J. Liu, X. C. Xie, J. Wei, and J. Wang, Nat. Mater. **15**, 38 (2016)

[12] M. Neupane, N. Alidoust, S.-Y. Xu, T. Kondo, Y. Ishida, D. J. Kim, C. Liu, I. Belopolski, Y. J. Jo, T.-R. Chang *et al.*, Nat. Commun. **4**, 2991 (2013).

[13] B.-J. Yang and N. Nagaosa, Nat. Commun. **5**, 4898 (2014).

[14] S. M. Young and C. L. Kane, Phys. Rev. Lett. **115**, 126803 (2015).

[15] S.-M. Huang, S.-Y. Xu, I. Belopolski, C.-C. Lee, G. Chang, B. Wang, N. Alidoust, G. Bian, M. Neupane, C. Zhang *et al.*, Nat. Commun. **6**, 7373 (2015).

[16] H. Weng, C. Fang, Z. Fang, B. A. Bernevig, and X. Dai, Phys. Rev. X **5**, 011029 (2015).

[17] S.-Y. Xu, I. Belopolski, N. Alidoust, M. Neupane, G. Bian, C. Zhang, R. Sankar, G. Chang, Z. Yuan, C.-C. Lee *et al.*, Science **349**, 613 (2015).

[18] B. Q. Lv, H. M. Weng, B. B. Fu, X. P. Wang, H. Miao, J. Ma, P. Richard, X. C. Huang, L. X. Zhao, G. F. Chen, Z. Fang, X. Dai, T. Qian, and H. Ding, Phys. Rev. X **5**, 031013 (2015).

[19] M. Z. Hasan, S.-Y. Xu, and G. Bian, Phys. Scr. **T164**, 014001 (2015).

[20] A. A. Burkov, M. D. Hook, and L. Balents, Phys. Rev. B **84**, 235126 (2011).

[21] M. Phillips and V. Aji, Phys. Rev. B **90**, 115111 (2014).

[22] H. Weng, Y. Liang, Q. Xu, R. Yu, Z. Fang, X. Dai, and Y. Kawazoe, Phys. Rev. B **92**, 045108 (2015).

[23] Y. Kim, B. J. Wieder, C. L. Kane, and A. M. Rappe, Phys. Rev. Lett. **115**, 036806 (2015).

[24] L. S. Xie, L. M. Schoop, E. M. Seibel, Q. D. Gibson, W. Xie, and R. J. Cava, APL Mater. **3**, 083602 (2015).

[25] Q. Xu, Z. Song, S. Nie, H. Weng, Z. Fang, and X. Dai, Phys. Rev. B **92**, 205310 (2015).

[26] L. M. Schoop, M. N. Ali, C. Straber, V. Duppel, S. S. P. Parkin, B. V. Lotsch, and C. R. Ast, Nat. Commun. **7**, 11696 (2016).

[27] M. Neupane, I. Belopolski, M. M. Hosen, D. S. Sanchez, R. Sankar, M. Szlawska, S.-Y. Xu, K. Dimitri, N. Dhakal, P. Maldonado, P. M. Oppeneer, D. Kaczorowski, F. C. Chou, M. Z. Hasan, and T. Durakiewicz, Phys. Rev. B **93**, 201104 (2016).

[28] R. Lou, J.-Z. Ma, Q.-N. Xu, B.-B. Fu, L.-Y. Kong, Y.-G. Shi, P. Richard, H.-M. Weng, Z. Fang, S.-S. Sun, Q. Wang, H.-C. Lei, T. Qian, H. Ding, and S.-C. Wang, Phys. Rev. B **93**, 241104(R) (2016).

[29] Y.-Y Lv, B.-B. Zhang, X. Li, S.-H. Yao, Y. B. Chen, J. Zhou, S.-T. Zhang, M.-H. Lu, and Y.-F. Chen, Appl. Phys. Lett. **108**, 244101 (2016).

[30] Z. Wang, Y. Sun, X.-Q. Chen, C. Franchini, G. Xu, H. Weng, X. Dai, and Z. Fang, Phys. Rev. B **85**, 195320 (2012).

[31] Z. K. Liu, B. Zhou, Z. J. Wang, H. M. Weng, D. Prabhakaran, S.-K. Mo, Y. Zhang, Z. X. Shen, Z. Fang, X. Dai *et al.*, Science **343**, 864 (2014).

[32] S.-Y. Xu, C. Liu, S. K. Kushwaha, R. Sankar, J. W. Krizan, I. Belopolski, M. Neupane, G. Bian, N. Alidoust, T. R. Chang *et al.*, Science **347**, 294 (2015).

[33] J. Xiong, S. K. Kushwaha, T. Liang, J. W. Krizan, M. Hirschberger, W. Wang, R. J. Cava, and N. P. Ong, Science **350**, 413 (2015).

[34] M. Neupane, N. Alidoust, M. M. Hosen, J.-X. Zhu, K. Dimitri, S.-Y. Xu, N. Dhakal, R. Sankar, I. Belopolski, D. S. Sanchez *et al.*, Nat. Commun. **7**, 13315 (2016).

[35] M. Neupane, M. M. Hosen, I. Belopolski, N. Wakeham, K. Dimitri, N. Dhakal, J.-X. Zhu, M. Z. Hasan, E. D. Bauer, and F. Ronning, J. Phys.: Condens. Matter **28**, 23LT02 (2016).

[36] M. N. Ali, J. Xiong, S. Flynn, J. Tao, Q. D. Gibson, L. M. Schoop, T. Liang, N. Haldolaarachchige, M. Hirschberger, N. P. Ong, and R. J. Cava, Nature (London) **514**, 205 (2014).

[37] Y. Zhao, H. Liu, J. Yan, W. An, J. Liu, X. Zhang, H. Wang, Y. Liu, H. Jiang, Q. Li, Y. Wang, X.-Z. Li, D. Mandrus, X. C. Xie, M. Pan, and J. Wang, Phys. Rev. B **92**, 041104(R) (2015).

[38] A. A. Soluyanov, D. Gresch, Z. Wang, Q. Wu, M. Troyer, X. Dai, and B. B. Bernevig, Nature (London) **527**, 495 (2015).

[39] M. Luscher, Phys. Lett. B **428**, 342 (1998).

[40] J. Fröhlich and B. Pedrini, arXiv:hep-th/0002195.

[41] T. Liang, Q. Gibson, M. N. Ali, M. Liu, R. J. Cava, and N. P. Ong, Nat. Mater. **14**, 280 (2015).

[42] H. Wang, C.-K. Li, H. Liu, J. Yan, J. Wang, J. Liu, Z. Lin, Y. Li, Y. Wang, L. Li, D. Mandrus, X. C. Xie, Ji Feng, and J. Wang, Phys. Rev. B **93**, 165127 (2016).

[43] G. Bian, T.-R. Chang, R. Sankar, S.-Y. Xu, H. Zheng, T. Neupert, C.-K. Chiu, S.-M. Huang, G. Chang, I. Belopolski *et al.*, Nat. Commun. **7**, 10556 (2016).

[44] Y. Wu, L.-L. Wang, E. Mun, D. D. Johnson, D. Mou, L. Huang, Y. Lee, S. L. Bud'ko, P. C. Canfield, and A. Kaminski, Nat. Phys. **12**, 667 (2016).

[45] J. Hu, Z. Tang, J. Liu, X. Liu, Y. Zhu, D. Graf, K. Myhro, S. Tran, C. N. Lau, J. Wei, and Z. Mao, Phys. Rev. Lett. **117**, 016602 (2016).

[46] C. Wang and T. Hughbanks, Inorg. Chem. **34**, 5524 (1995).

[47] R. Singha, A. K. Pariari, B. Satpati, and P. Mandal, Proc. Natl. Acad. Sci. USA **114**, 2468 (2017).

[48] G. Kresse and J. Furthmüller, Phys. Rev. B **54**, 11169 (1996).

[49] G. Kresse and J. Hafner, Phys. Rev. B **48**, 13115 (1993).

[50] J. P. Perdew, K. Burke, and M. Ernzerhof, Phys. Rev. Lett. **77**, 3865 (1996).

[51] G. Kresse and D. Joubert, Phys. Rev. B **59**, 1758 (1999).

[52] F. F. Tafti, Q. D. Gibson, S. K. Kushwaha, N. Haldolaarachchige, and R. J. Cava, Nat. Phys. **12**, 272 (2016).

[53] D. Wu, J. Liao, W. Yi, X. Wang, P. Li, H. Weng, Y. Shi, Y. Li, J. Luo, X. Dai, and Z. Fang, Appl. Phys. Lett. **108**, 042105 (2016).

[54] Y. L. Wang, L. R. Thoutam, Z. L. Xiao, J. Hu, S. Das, Z. Q. Mao, J. Wei, R. Divan, A. Luican-Mayer, G. W. Crabtree, and W. K. Kwok, Phys. Rev. B **92**, 180402(R) (2015).

[55] See Supplemental Material at http://link.aps.org/supplemental/10.1103/PhysRevB.95.161101 for more photon energy dependent Fermi surface maps of ZrSiTe and further discussion of the experimental observations.